Combining spectral induced polarization with x-ray tomography to investigate the importance of DNAPL geometry in sand samples

Johansson, Sara; Rossi, Matteo; Hall, Stephen; Sparrenbom, Charlotte J.; Hagerberg, David; Tudisco, Erika; Rosqvist, Håkan; Dahlin, Torleif

Published in:
Geophysics

DOI:
10.1190/geo2018-0108.1

2019

Document Version:
Publisher's PDF, also known as Version of record

GEOPHYSICS, VOL. 84, NO. 3 (MAY-JUNE 2019); P. E173–E188, 12 FIGS., 3 TABLES.
10.1190/GEO2018-0108.1

Combining spectral induced polarization with X-ray tomography to investigate the importance of DNAPL geometry in sand samples

Sara Johansson[1], Matteo Rossi[1], Stephen A. Hall[2], Charlotte Sparrenbom[3], David Hagerberg[4], Erika Tudisco[5], Håkan Rosqvist[3], and Torleif Dahlin[1]

ABSTRACT

Although many studies have been performed to investigate the spectral induced polarization (SIP) response of nonaqueous phase liquid (NAPL)-contaminated soil samples, there are still many uncertainties in the interpretation of the data. A key issue is that altered pore space geometries due to the presence of a NAPL phase will change the measured IP spectra. However, without any information on the NAPL distribution in the pore space, assumptions are necessary for the SIP data interpretation. Therefore, experimental data of SIP signals directly associated with different NAPL distributions are needed. We used high-resolution X-ray tomography and 3D image processing to quantitatively assess NAPL distributions in samples of fine-grained sand containing different concentrations of tetrachloroethylene and link this to SIP measurements on the same samples. The total concentration of the sample constituents as well as the volumes of the individual NAPL blobs were calculated and used for the interpretation of the associated SIP responses. The X-ray tomography and image analysis showed that the real sample properties (porosity and NAPL distributions) differed from the targeted ones. Both contaminated samples contained less NAPL than expected from the manual sample preparation. The SIP results showed higher real conductivity and lower imaginary conductivity in the contaminated samples compared to a clean sample. This is interpreted as an effect of increased surface conductivity along interconnected NAPL blobs and decreased surface areas in the samples due to NAPL blobs larger than and enclosing grains. We conclude that the combination of SIP, X-ray tomography, and image analysis is a very promising approach to achieve a better understanding of the measured SIP responses of NAPL-contaminated samples.

INTRODUCTION

Laboratory research focusing on the spectral induced polarization (SIP) response of nonaqueous phase liquid (NAPL)-contaminated samples has been carried out by many different research groups during the past few decades (e.g., Olhoeft, 1985; Börner et al., 1993; Vanhala, 1997; Martinho et al., 2006; Cassiani et al., 2009; Schmutz et al., 2010; Revil et al., 2011; Schwartz et al., 2012; Ustra et al., 2012; Shefer et al., 2013). The large number of laboratory studies in this field can be explained by the need of obtaining a better understanding of the measured electrical response of controlled samples. The interpretation of NAPL-contaminated samples is, however, complex even in a laboratory setting. No consensus has been reached between different studies about the expected SIP response of a NAPL-contaminated soil (Johansson et al., 2015). One major issue is that the oil-like NAPL contaminants exist as a separate phase in the pore system, and it is unknown how the NAPLs interact geometrically with grain surfaces and change the pore system. Interpretation of laboratory data has, therefore, often relied on conceptual models of the geometry of the three-phase system in the samples (Olhoeft, 1985; Titov et al., 2004; Martinho et al., 2006; Schmutz et al., 2010; Revil et al., 2011; Shefer et al.,

Manuscript received by the Editor 15 February 2018; revised manuscript received 11 January 2019; published ahead of production 13 February 2019; published online 29 March 2019; corrected version published online 9 April 2019.
[1]Lund University, Division of Engineering Geology, Lund, Sweden. E-mail: sara.johansson@tg.lth.se (corresponding author); matteo.rossi@tg.lth.se; torleif.dahlin@tg.lth.se.
[2]Lund University, Division of Solid Mechanics, Lund, Sweden. E-mail: stephen.hall@solid.lth.se.
[3]Lund University, Department of Geology, Lund, Sweden. E-mail: charlotte.sparrenbom@geol.lu.se; hakan.rosqvist@geol.lu.se.
[4]Tyrens AB, Malmö, Sweden. E-mail: david.hagerberg@tyrens.se.
[5]Lund University, Division of Geotechnical Engineering, Lund, Sweden. E-mail: erika.tudisco@construction.lth.se.

2013). Johansson et al. (2015) review different possible NAPL configurations in a granular pore space and discuss how these conceptual NAPL configurations would be expected to change the IP spectra based on the current understanding of different IP mechanisms. In this work, it was concluded that different NAPL configurations in the pore space might explain why the SIP results from different studies in previous research are inconsistent. In a recent study by Bücker et al. (2017), analytical modeling provides mechanistic support for varying SIP responses with different geometric NAPL configurations.

The main objective of the current study is to recreate, in a real sample, some of the conceptual NAPL configurations presented by Johansson et al. (2015) and to test the hypotheses of how different NAPL configurations affect the measured IP spectra. We use a sample preparation method based on manual mixing of sand and NAPL because this is the most common approach in previous research (see, e.g., Martinho et al., 2006; Schmutz et al., 2010, 2012; Revil et al., 2011; Schwartz et al., 2012; Ustra et al., 2012; Shefer et al., 2013). The dense NAPL (DNAPL) species tetrachloroethylene (PCE) is considered because this is a common contaminant (e.g., from old dry cleaners), and efficient field site investigation methods for the detection of PCE spills are needed (see, e.g., Johansson et al., 2015).

It is well-known that IP mechanisms arise at the pore scale (e.g., Kemna et al., 2012); therefore, an altered pore space due to the NAPL phase will change the measured IP spectra. However, we expect that the NAPL configuration in the pore space is difficult to control during sample preparation, especially when manual sample preparation methods are used. Therefore, in this work, a novel combination of SIP measurements and high-resolution X-ray tomography on the same samples is used to assess the actual configuration of the NAPL and the associated SIP signal. The high-resolution X-ray tomography enables visualization and quantification at the pore scale thus removing the need to assume that a certain NAPL distribution has been achieved; the actual configuration can be characterized instead. Furthermore, sample properties that are considered to influence the SIP signal can be calculated from the images.

The importance of knowing the NAPL distribution in samples for interpretation of measured SIP responses has been previously stressed by Cassiani et al. (2009). Cassiani et al. (2009) use X-ray tomography to measure the bulk distribution of NAPLs in their SIP investigated samples. However, the low-resolution tomography used only enabled a measurement of density variations in the samples, but it did not allow any detailed inspection of the NAPL configurations in the pore space. Quantification of sample properties from X-ray tomography images is a new method for interpretation of SIP data; as far as we know, only a limited amount of studies have been presented yet as conference abstracts (Johansson et al., 2017a, 2017b; Kruschwitz et al., 2017; Zhang et al., 2017).

The use of high-resolution X-ray tomography in the geosciences is not new. The technique has been successfully applied to a range of problems within the geosciences; see, e.g., the reviews from Cnudde and Boone (2013), Ketcham and Carlson (2001), and Wildenschild and Sheppard (2013). One of the geoscientific applications is to use high-resolution X-ray tomography to investigate details such as the shapes, configuration, and flow mechanisms of NAPLs in porous materials (Turner et al., 2004; Willson et al., 2004; Al-Raoush and Willson, 2005; Culligan et al., 2006). Different NAPL species have been investigated in these studies, including PCE (Schnaar and Brusseau, 2006; Goldstein et al., 2007; Brusseau et al., 2008).

In contrast to the above-mentioned studies using X-ray tomography to characterize NAPL distributions, in this work the tomography imaging is performed on samples that are also measured with SIP. This implies some extra experimental constraints regarding the sample holder dimensions and X-ray scanning time to realize the combination of X-ray tomography and SIP measurements on the same samples. Another difficulty was that chemical dopants could not be used to increase the X-ray attenuation contrast of the NAPL because it is unknown how the dopant would affect the electrical and physical properties of the fluid.

The aim of this work is to provide new insights about both the interpretation of SIP spectra measured on NAPL-contaminated samples and sample preparation methods. The theoretical background of SIP measurements is first reviewed before describing the experimental methods and data analysis. The X-ray tomography and SIP results are presented before the SIP and X-ray data are interpreted together to draw conclusions on how the NAPL configuration affects the SIP signal.

We believe that the combination of SIP, X-ray tomography, and image analysis is a very promising approach to move forward with a better understanding of the measured SIP responses of NAPL-contaminated samples. Such an understanding also improves the interpretation of spectral IP data measured at NAPL-contaminated field sites.

THEORETICAL BACKGROUND

SIP measurements carried out in the frequency domain are based on the principle of injecting an alternating current (AC) between two electrodes in contact with the sample material. The electrical potential in the sample is simultaneously measured across a second pair of electrodes, which returns the amplitude ($|\rho|$) and phase shift (φ) of the received AC potential in relation to the injected current. The measurements are repeated over a range of AC frequencies, usually in between 0.01 and 1000 Hz, which results in amplitude and phase spectra showing the spectral response of the sample material to the injected current frequencies. The complex conductivity (σ^*) measured with frequency-domain systems can be expressed as

$$\sigma^* = \frac{1}{|\rho|} e^{-i\varphi} = \sigma' + i\sigma'', \tag{1}$$

where σ' is the real part and σ'' is the imaginary part of the complex conductivity σ^*.

The SIP amplitude spectrum is related to the electrical resistivity (or its reciprocal conductivity) of the sample, whereas the phase spectrum is a measure of the electrical polarization of the sample. The main part of this polarization, also referred to as the IP effect, arises in metal-free sands when charges are not able to move freely with the electrical current. Such charges can be blocked in front of narrow passages in the pore system or can be attached to grain surfaces in the electrical double layer (EDL). Two different mechanistic frameworks exist for explaining and quantifying (for simple approximations of geologic microstructures) the low-frequency IP effect in metal-free geologic materials: the membrane polarization mechanism and the electrochemical polarization mechanism. There is currently no consensus in the research field about which

of these two polarization mechanisms that better describe spectral IP effects in geologic materials, and it is possible that both mechanisms exist simultaneously. Therefore, both mechanisms will be introduced here and both are used to interpret the experimental results in the "Discussion" section.

The membrane polarization mechanism, which was first suggested by Marshall and Madden (1959), is based on the idea that zones of different ion transparency exist in geologic materials, e.g., clayey ion-selective zones or narrow pore throats. Ions are blocked in front of these zones when an electrical field is applied, which leads up to charge accumulations. The magnitude of the charge accumulation is dependent on the distance between zones of different ion transparency, and the existence of these different zones is a prerequisite for any IP effects to occur at all (Marshall and Madden, 1959). In membrane polarization models of granular materials, the length distribution of pore throats or pores, working as ion-selective and nonselective zones, control the relaxation time of the polarization (Titov et al., 2002; Bücker and Hördt, 2013).

The electrochemical polarization mechanisms arise when ions in the fixed layer of the EDL are displaced under the influence of an electrical field (Schwarz, 1962). In addition to the inner and strongly attached fixed layer, the EDL also consists of an outer and weakly attached layer called the diffuse layer. It is mainly the displacement of the fixed layer that gives rise to IP effects in granular materials; the diffuse layer is often considered continuous over neighboring grains and therefore only contributes to surface conduction (Leroy et al., 2008; Revil and Florsch, 2010). In electrochemical polarization models, smaller grain sizes produce larger polarization magnitudes and shorter relaxation times compared to larger grain sizes (e.g., Revil and Florsch, 2010).

As shown by, e.g., Slater and Lesmes (2002), the electrical conduction and the ionic polarization processes described above can be viewed as two parallel conduction paths in the pore system. In a water-saturated medium, the main part of the electrical conduction is transferred by ions in the pore fluid, whereas the polarization of ions requires that some of the current is also transported along the EDLs of the grains in the sample. In the case of a sample material with high porosity and high pore fluid salinity, most of the current will be transported by ionic conduction through the pore fluid and the phase response will, therefore, be weaker (Slater and Lesmes, 2002). That is, higher pore fluid salinity will lead to weaker phase response even though the electrical properties of the grain surfaces are the same. Slater and Lesmes (2002) show that the imaginary part σ'' can be approximated by

$$\sigma'' \cong \varphi \cdot \sigma', \tag{2}$$

for $\sigma'' \ll \sigma'$. So, the imaginary part σ'' is the phase angle normalized by the conductivity of the sample. The effect of the normalization is to neutralize the dependence of the phase parameter on the bulk pore fluid salinity. Therefore, the imaginary part can be interpreted as a parameter that only represents the polarization of charges along surfaces in the sample.

The complex response of a material to alternating electric fields is determined not only by the complex conductivity σ^* but also by the complex dielectric permittivity ε^* of the material, which becomes increasingly important as the AC frequency is increased. The complex dielectric permittivity is a measure of the ability of the material to obtain an intrinsic electrical polarization, where the real part ε' describes the electrical energy storage (polarization) and the imaginary part ε'' describes the energy loss from electrical conduction. The complex dielectric permittivity is related to the complex conductivity (e.g., de Lima and Sharma, 1992) as

$$\sigma^* = i\omega\varepsilon^* = -\omega\varepsilon'' + i\omega\varepsilon', \tag{3}$$

where ω is the angular frequency. Equation 3 shows that the imaginary part of the complex conductivity is increasingly affected by the real part of the complex dielectric permittivity of the sample as the frequency increases. That is, the SIP effect cannot be measured without also measuring the frequency dispersion of the real part of the dielectric permittivity ε'.

In summary, the measured real conductivity (σ') can be interpreted as the bulk electrical conductivity of the sample, whereas the imaginary conductivity (σ'') is a measure of the total electrical polarization in the sample. The total electrical polarization consists of a superposition of two types of electromagnetic interactions: (1) ionic, i.e., polarization of ions with restricted mobility in the pore water (referred to as the IP effect), and (2) dielectric, i.e., intrinsic polarization of the sample materials caused by their ability to store electrical energy by alignment of atoms or molecules (quantified by their real-valued dielectric permittivity ε'). The ionic relaxation processes, or SIP effect, can consist of the electrochemical and/or membrane polarization mechanisms described above. At high frequencies, they can also be influenced by the Maxwell-Wagner polarization, which is an ionic charge separation that occurs at interfaces between materials with different conductivity and permittivity.

METHODS AND MATERIALS

The objective of the experiments in this study was to investigate how the distribution and configuration of the NAPL PCE in sand samples affect measured SIP responses. A major drawback with using PCE in SIP laboratory experiments is that it reacts aggressively and rapidly when in contact with certain materials, e.g., plastics. For this reason, a sample holder of glass, which is stable against PCE, was developed for this experiment. PCE is also a volatile and toxic chemical. Practical laboratory work with PCE therefore demands careful handling as well as awareness of safety issues and risk assessments. Naturally, these issues lead to practical limitations to the experiments. Due to safety issues and national regulations, the major part of the experimental work was carried out under a fume hood. To avoid skin contact, thick gloves were used during the sample preparations. To transport and contain the contaminated samples in the X-ray tomography laboratory, silicon was used to seal all openings of the sample holders, e.g., the potential electrode channels (see Figure 1b). In addition, the sample holder was mounted in an external glass cylinder to eliminate the risk of PCE leakage into the X-ray tomograph (Figure 1c). The lid of the cylinder was sealed to the cylinder by using silicon, Parafilm, and metal film to eliminate any risk of gas escaping from the sample.

To realize the combination of SIP measurements and high-resolution X-ray tomography on the same samples, special sample holders were designed with the requirements that they should follow geometric recommendations for measuring high-quality SIP data (Zimmermann et al., 2008) and have small enough diameters to enable high-resolution X-ray tomography of the full sample width over reasonable timescales. The sample holders should also be able to withstand exposure to PCE, which is why they are manu-

factured and they should be X-ray transparent. A photograph of the sample holder is shown in Figure 1b, and Figure 1a shows a sketch of the sample holder dimensions. The lengths and diameters of the sample holders are 16 and 2.4 cm, respectively. Current plate electrodes of stainless steel are used at each end of the cylinder, and the channels for potential electrodes are placed 6 cm from each current electrode. The potential electrodes are made of copper and are extracted from the current path using drilled rubber lids. The contact medium between the potential electrode and the sample is agar-agar gel made from the same electrolyte used in the sample.

The targeted sample properties investigated in this study are shown in Table 1. A medium-grained sand with grain sizes ranging from 250 to 355 μm was used for the experiments. The sand was chosen because SIP measurements resulted in repeatable and distinct Cole-Cole-shaped spectra serving as appropriate background signals for the experiments. The grain size distribution of the sand is also appropriate for the resolution of the X-ray tomography imaging performed in this study. Petrographic data from the sand provider show that it consists of 74% quartz, 24% feldspar, and 2% mica. A sodium chloride (NaCl) electrolyte with a conductivity of 10 mS/m was prepared from deionized water and salt, and the sand was packed in the sample holder with a glass rod. The low salinity was chosen to increase the signal strength of the phase data. To ensure water-saturated conditions, the electrolyte surface was kept slightly higher than the surface of the packed sand during the major part of the sample preparation.

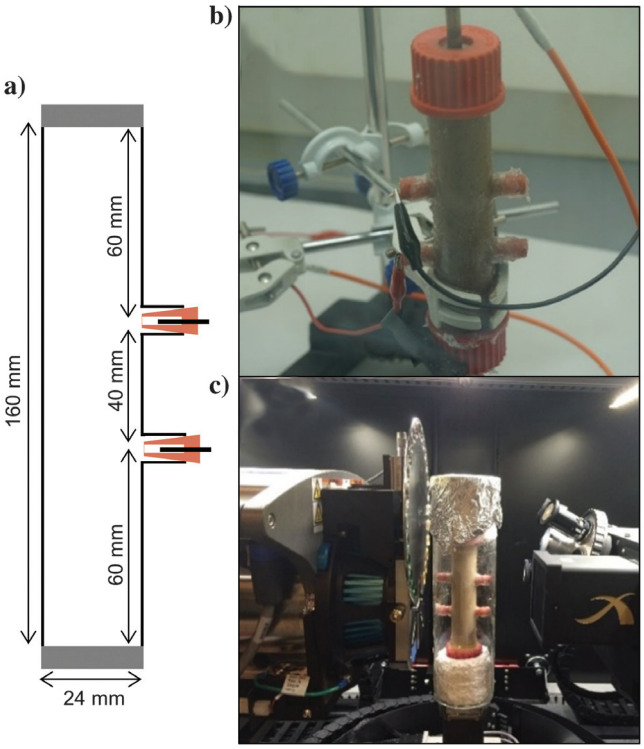

Figure 1. (a) Sketch of the sample holder design. (b) Photograph showing the sample holder during the SIP measurements under the fume hood. The sample holder has four potential electrode channels, but only two of them were used for the measurements. (c) Photograph of the sample holder contained in an external air-sealed glass cylinder during the X-ray tomography.

The porosity of the clean sand sample was estimated from the weight of the dry sand, the weight of the dry sample holder, and the total weight of the water-saturated sample prepared in the sample holder. From these measurements, the volumetric water content was then determined and used as a measure of the sample porosity. Repeated preparations of replicas showed that the packing method resulted in sample porosities of approximately 34%–35%. The expected pore volume of the sand after packing can therefore be considered to be known. This value was used to calculate the required amount of PCE for the mixture to obtain a PCE concentration of approximately 10 vol% and 40 vol% of the pore space (samples PCE1 and PCE2 in Table 1). To obtain water-wet conditions in the samples, the required mass amount of dry sand was mixed with small amounts of electrolyte in a beaker until the sand was moist. The selected amount of PCE was then added to the moist sand and manually mixed before the sample holder was packed with the mixture according to the same method described above.

The main experimental procedure for each contaminated sample consists of the following steps:

- preparation of the sample holder and potential electrodes
- control measurements on the electrolyte
- sample preparation and packing under a fume hood
- SIP measurements under a fume hood
- enclosure of the sample holder in an air-sealed glass cylinder
- X-ray tomography
- unsealing of the sample holder under a fume hood
- replication of SIP measurements under a fume hood
- destruction of the sample and decontamination of the sample holder.

A similar experimental procedure was used for the clean sand sample, with the exception that the sample holder was not enclosed in the air-sealed glass cylinder during the X-ray tomography.

SIP measurements and data analysis

The SIP measurements were performed with a ZWL-SIP04 impedance meter in the frequency range of 0.01–1000 Hz (Zimmermann et al., 2008). The measurement protocol took less than 1 h to complete, which was considered an acceptable time range for the contaminated samples. During this time, no major chemical interactions were expected to occur in PCE1 and PCE2. The clean sand sample was also measured in the broader frequency range of 0.001–1000 Hz that took more than 8 h to complete, a time scale that was not acceptable for the contaminated samples. The extended frequency range of the clean sand sample was motivated by the minor risk of chemical interactions within the sample and absent risk of toxic gas leakage through the sample holder. Furthermore, the investment in the X-ray tomography investigation of the clean sand

Table 1. Summary of the targeted sample properties.

Sample	Porosity	PCE saturation	Water saturation
Clean	34%–35%	0%	100%
PCE1	34%–35%	10%	90%
PCE2	34%–35%	40%	60%

sample motivated measurements of SIP data sets that were as comprehensive as possible.

The measurement accuracy of the SIP setup was tested with a 1 k Ω resistor as well as with measurements on pure electrolyte to ensure that no spurious phase values from the sample holders or electrodes were recorded. Several replicas of clean and water-saturated sand samples were prepared, and the SIP results on these replicas ensured repeatability in the measurements. All SIP measurements were performed at a temperature of 20°C–21°C, whereas the temperature in the tomograph was 28°C.

A common way to describe the results measured with SIP is to fit the phase data with a phenomenological model and extract the model parameters. The most commonly used phenomenological model for this purpose is the Cole-Cole model (Pelton et al., 1978):

$$\rho^*(\omega) = \rho_0\left[1 - m_0\left(1 - \frac{1}{1 + (i\omega\tau)^c}\right)\right], \qquad (4)$$

where $\rho^*(\omega)$ is the complex resistivity as a function of frequency and ρ_0 is the low-frequency limit of resistivity. The chargeability m_0 (mV/V), relaxation time τ (s), and frequency exponent c (unitless) are the Cole-Cole parameters. The Cole-Cole model assumes a spectrum with a single phase peak described by the parameters τ and c in terms of position and width on the frequency axis. In this study, we used a double Cole-Cole model to fit the phase data. The use of multiple Cole-Cole models for fitting data is based on the assumption of several superimposed Cole-Cole-like relaxations in the phase spectrum, an approach that was also used by Pelton et al. (1978).

The Cole-Cole parameters of the relaxation at the lower frequency end are used to describe the electrochemical or membrane polarization mechanism in our samples. To analyze data at the high-frequency end of the phase spectra, we use mixing models to calculate the dielectric permittivity of the samples. For the contaminated samples, we follow the method presented by Brovelli and Cassiani (2010) to calculate the dielectric response of a three-phase mixture based on the Hashin-Shtrikman bounds and Archie's law (Archie, 1942). For the clean sand sample, we use the Brovelli and Cassiani approach for a two-phase mixture as well as the permittivity low-frequency limit of the Bruggeman-Hanai-Sen effective medium mixing model (Sen et al., 1981). For both approaches, we use values of 80 and 4.5 for the relative dielectric permittivity of the water and sand, respectively (Brovelli and Cassiani, 2010). For the three-phase mixture, we use a value of 2.29 for the dielectric constant of PCE (Ajo-Franklin et al., 2006). For water conductivity and porosity, the same values as in the experiments were used. When applicable, the value for the Archie saturation exponent n was set to 2.0 (Archie, 1942). The Archie cementation exponent m was adjusted so that the corresponding bulk conductivity value matched the measured values for the clean sample.

X-ray tomography and image analysis

In X-ray tomography, the sample is exposed to X-rays from different angles during a 360° rotation. The X-rays are transmitted through the sample in which they interact with the matter and become attenuated. The transmitted X-rays are recorded by a 2D detector providing radiographs, which can be used to reconstruct a 3D volume of the linear attenuation coefficients in the sample. The linear attenuation coefficient depends on the energy of the beam as well as the electron density and mass density of the sample material. It is the differences in linear attenuation coefficient between different materials that makes them distinguishable in X-ray tomography. The spatial resolution of the reconstructed X-ray tomography depends on the type of equipment used, the distances between the X-ray source, the sample, and the detector, and the signal-to-noise ratio in the data. The signal-to-noise ratio can be increased by increasing the exposure time or the incident radiation intensity on the sample. High spatial resolution generally requires longer exposure times. For more details about the X-ray tomography method, the reader is referred to, e.g., Wildenschild and Sheppard (2013).

The X-ray tomography in this study was performed at the 4D imaging Lab at Lund University with a ZEISS XRM520. The X-ray source is a polychromatic cone beam, and a source voltage of 160 kV, a power of 10 W, and an exposure time of 6 s was used for the contaminated samples PCE1 and PCE2. A source voltage of 100 kV, power of 6 W, and exposure time of 6 s was used for the clean sand sample. An HE1 filter (as provided by the manufacturer) was used in between the X-ray source and the sample to reduce beam-hardening artifacts. The glass walls of the sample holder and the external glass cylinder enclosing the PCE1 and PCE2 samples also act as additional filters. The full cross section of the sample holders was scanned over a height of approximately 2 cm. The imaged volumes were centered in between the potential electrodes in the middle of the cylindrical sample holder (Figure 1). Radiographs from 1601 angles were measured during the 360° projection, and the voxel sizes of the reconstructed image stacks are 15 μm for PCE1 and PCE2 and 13 μm for the clean sand.

Despite the large mass density contrast between the PCE and the sand grains, the intensity contrast between these materials is low in the reconstructed images. The explanation for the low contrast can be found in the variation with the incident X-ray energy of the X-ray attenuation coefficients for PCE (C_2Cl_4) and quartz grains (SiO_2). The linear attenuation coefficients in Figure 2a were calculated with the online tool NIST-XCOM (Berger et al., 2010) and multiplied by the mass density values for PCE (1.59 g/cm^3), quartz grains (2.66 g/cm^3), and water (1.0 g/cm^3), respectively. The linear attenuation coefficient of a material is dependent on the electron density and the atomic number, with the latter becoming increasingly important as the energy decreases. Figure 2a shows that the attenuation coefficient of PCE theoretically exceeds that of quartz sand at

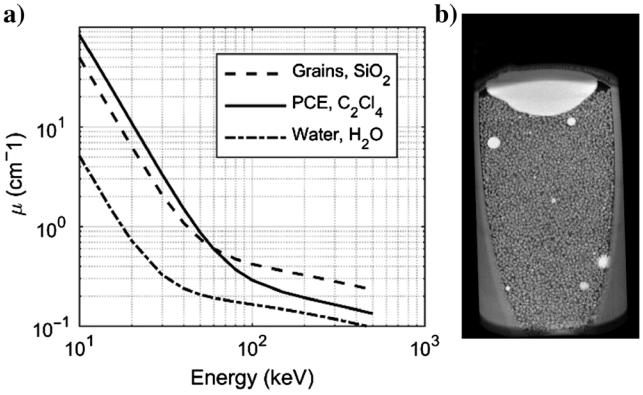

Figure 2. (a) Variation of X-ray attenuation coefficients with incident energy for the sample constituents quartz grains (sand), PCE, and water. (b) Result of test tomography scanning with source voltage of 80 kV, resulting in maximum intensity <40 kV.

energies <60 kV (due to the higher atomic number of PCE), whereas it falls below the value of quartz sand at energies >60 kV (due to the lower electron density in PCE). The energy produced by X-ray tubes consists of a continuous Bremsstrahlung spectrum. Although the maximum energy of the X-rays is determined by the source voltage (in this case 160 kV), the energy spectrum is typically skewed toward the lower end of the continuum. The effective intensity is typically found at a value of less than half of the source voltage (in this case <80 kV; see, e.g., Ketcham and Carlson, 2001; Poludniowski, 2007). In our case, the effective intensity of the incident radiation seems to have coincided with a value close to the overlap at 60 kV in the attenuation coefficients of PCE and quartz grains. Figure 2b shows the result of a test tomography scanning of a smaller sample with the same constituents. In this case, a source voltage of 80 kV was used, which resulted in a maximum intensity in the energy range <40 kV. In this range, the attenuation coefficient of PCE is larger than quartz sand (Figure 2a), thus resulting in the higher intensity in the reconstructed images (Figure 2b).

The reconstructed images were processed in MATLAB 2015b in two dimensions. A schematic overview of the different processing steps is shown in Figure 3, and an example of the results in each step can be found in the supplementary information that can be accessed through the following link: S1. A Wiener filter was applied to the images, which uses a statistical approach to remove noise in each pixel based on the local mean and standard deviation in a neighborhood window. An advantage of the Wiener filter, over other noise filtering approaches, is that it preserves edges in the image, in contrast to, e.g., a median filter that blurs the interfaces between different objects in the images. The Wiener filtered images can then relatively easily be used to segment the air, water, and glass phases using manual intensity thresholds. However, the PCE and sand grains could not be successfully separated from each other due to their similar intensities in the images.

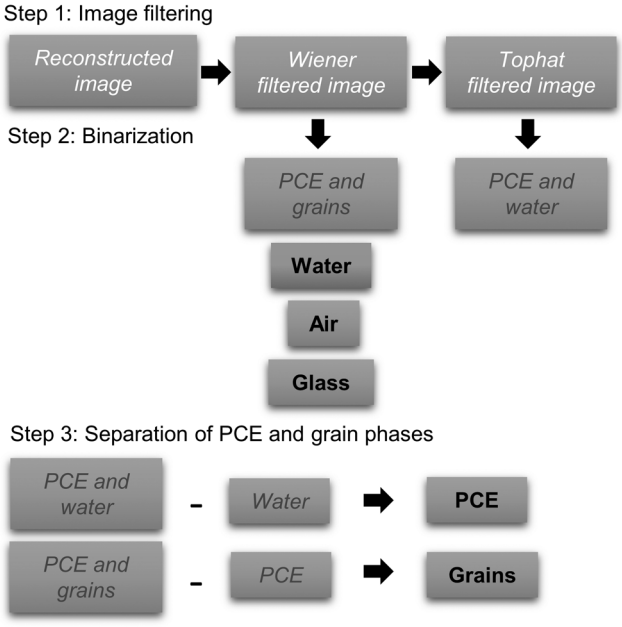

Figure 3. Schematic overview of the different image processing steps used to segment each phase in the sample.

To separate grains and PCE from each other in the images, a top-hat filter was first used. The top-hat filter uses pixel morphology (erosion and dilation) in a window of a user-specified size, such that bright areas larger than a specified size are identified and subtracted from the original image. In this case, the top-hat filtering operation suppresses bright regions larger than the size of a few grains; that is, individual grains keep high intensities in the resulting images while the larger regions containing PCE become dark (this, unfortunately, could result in some grains within PCE-filled regions being grouped with the PCE). A manual threshold could then be applied to the images to separate the dark PCE/water phases from the grains. To separate the PCE from the water phase, the top-hat filtered binary images were subtracted from the binary water images.

The images, segmented using the procedure described above, were used for 3D visualization as well as to calculate the relative amounts of the different phases via pixel counting. In addition, the volumes of the PCE blobs were calculated from the segmented PCE image stacks. It was assumed that segmented regions corresponding to 5 pixels or less correspond to image noise rather than PCE. Three-dimensional watershed segmentation was performed on the binary images from the clean sand sample to separate each individual grain in the image stack. This procedure enabled calculation of the grain volume distribution in the sample.

RESULTS

Initial inspection of the X-ray tomography images showed that the sample properties obtained in PCE1 and PCE2 differed from the targeted properties in Table 1. Therefore, qualitative descriptions and quantitative results, as obtained by image analysis of the X-ray tomography, are presented in the following and prior to the SIP measurement results.

Sample properties revealed by X-ray tomography

The X-ray tomography results consist of three image stacks representing the imaged volumes in between the potential electrodes of the clean sand sample, PCE1 and PCE2. Figure 4 shows a comparison of a section of an unprocessed image from the PCE2 image stack (Figure 4a) and the corresponding section after the image processing and segmentation (Figure 4b). As can be seen in Figure 4a, the level of detail is high in the reconstructed images and

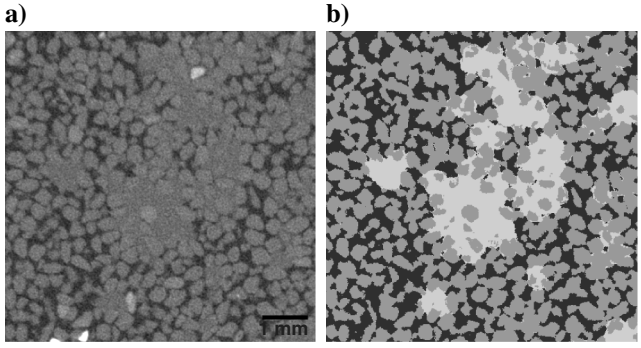

Figure 4. (a) Example section of an unprocessed image from sample PCE2. (b) The corresponding section after image processing and segmentation, as described in the main text.

grains and pores can easily be distinguished. However, the distribution of PCE is difficult to analyze due to its low intensity contrast relative to the grain intensity. On the other hand, in the segmented image in Figure 4b, the PCE distribution is clearly visualized and can be used to quantify the actual amount of PCE in the sample.

In general, image segmentation is a trade-off between visual details in the unprocessed images and the possibility to separate a single phase from the other phases and the background in the images. Segmentation reduces the information content of the images, and there are uncertainties in, for example, the choice of threshold intensity. In this case, however, the image filtering and segmentation resulted in grayscale images in which the PCE distribution is much more efficiently identified compared to a visual analysis. The comparison between unprocessed and segmented image sections, as in Figure 4, also shows that the distribution of the segmented PCE phase corresponds well to the patterns that can be identified by eye in the unprocessed image.

Selected images from the processed PCE1 and PCE2 image stacks are shown in Figures 5 and 6, respectively. Figure 5 shows examples of typical pore space conditions in sample PCE1. The pore space contained water, air voids, and PCE with the PCE phase mainly distributed as isolated blobs at various locations in the imaged volume. Figure 5a–5c shows examples of these typically isolated PCE blobs, whereas Figure 5d shows a region of sample PCE1 that contained many air voids.

Examples of typical PCE phase distributions in the pore space of sample PCE2 are shown in Figure 6. Sample PCE2 generally contained less air voids than sample PCE1, and the PCE phase was, in most cases, distributed as larger blobs with encapsulated grains. For example, a large interconnected PCE blob with encapsulated grains is visible in Figure 6b, whereas the PCE phase is located along the glass cylinder wall in Figure 6d. Smaller, isolated PCE blobs were also present in sample PCE2; examples of these are shown in Figure 6a and 6c.

Three-dimensional renderings of the segmented image stacks from both samples are shown in Figure 7, as well as in the digital ancillary files. It is clear that the preparation of the two samples with different PCE concentrations was successful, and that the grains are relatively well-packed. The 3D renderings also give an overview of the heterogeneity of the samples. Some packing effects can, for example, be observed in sample PCE2 as layers with different amounts of PCE (Figure 7b and 7d).

The qualitative observations reported so far are confirmed by the quantitative results from the image analysis shown in Table 2. The porosity in the clean sand sample was 37% according to the image analysis, whereas the porosity determined by the weight was 35%. Although there are uncertainties in both methods of estimating porosity, it is likely that the value calculated from the images is slightly overestimated due to, e.g., segmentation and discretization effects. Even so, the porosity determined for sample PCE1 of 44% is clearly far from the targeted value of 34%–35% (Table 1). In PCE2, the calculated porosity value is 40%, which confirms the qualitative observation that the preparation of sample PCE2 was more successful. Furthermore, the proportion of air in the pore space is calculated to be 4.4% in PCE1, whereas it is only 1.2% in sample PCE2.

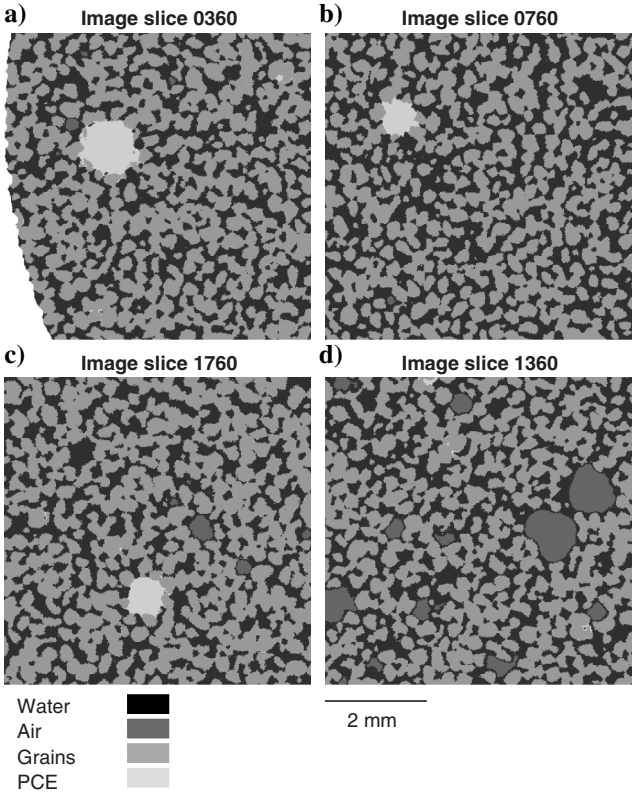

Figure 5. Examples of pore space distribution of phases in sample PCE1.

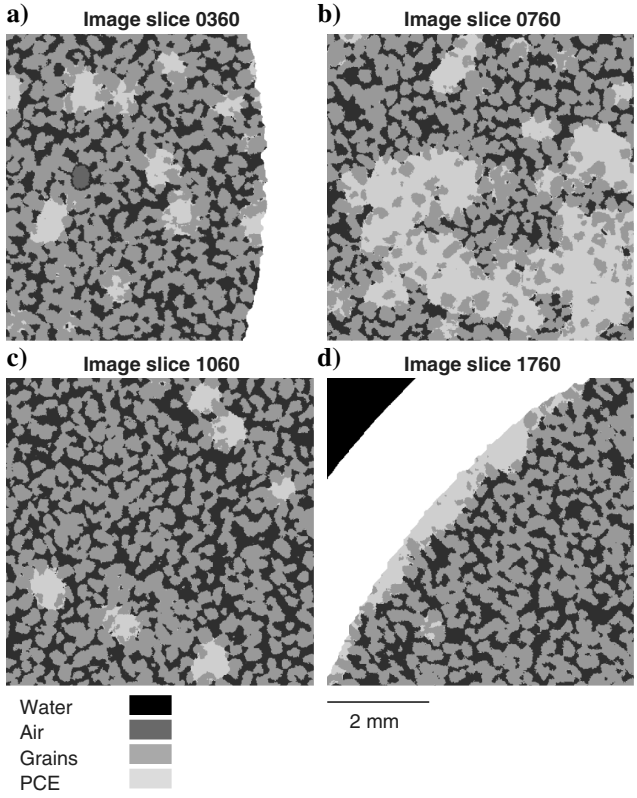

Figure 6. Examples of pore space distribution of phases in sample PCE2.

As expected, the pore space in sample PCE2 contained more PCE compared to PCE1. Calculated values of 11% and 1.5% of the pore space volume, respectively, are reported in Table 2, which confirms that the preparation of two samples with different PCE concentrations was successful. However, the actual amounts of PCE were much lower than expected for both samples. It is possible that the PCE concentrations in the samples differ in parts of the sample holders that were not covered by the X-ray tomography. However, the most likely explanation is that larger amounts of PCE than expected were left in the beaker after the manual mixing of the sample constituents. Furthermore, a significant amount of the added PCE might have vaporized during the sample preparations because PCE is a volatile chemical. Finally, uncertainties in the segmentation of the PCE phase might also account for a slight part of the discrepancy between the targeted and calculated values.

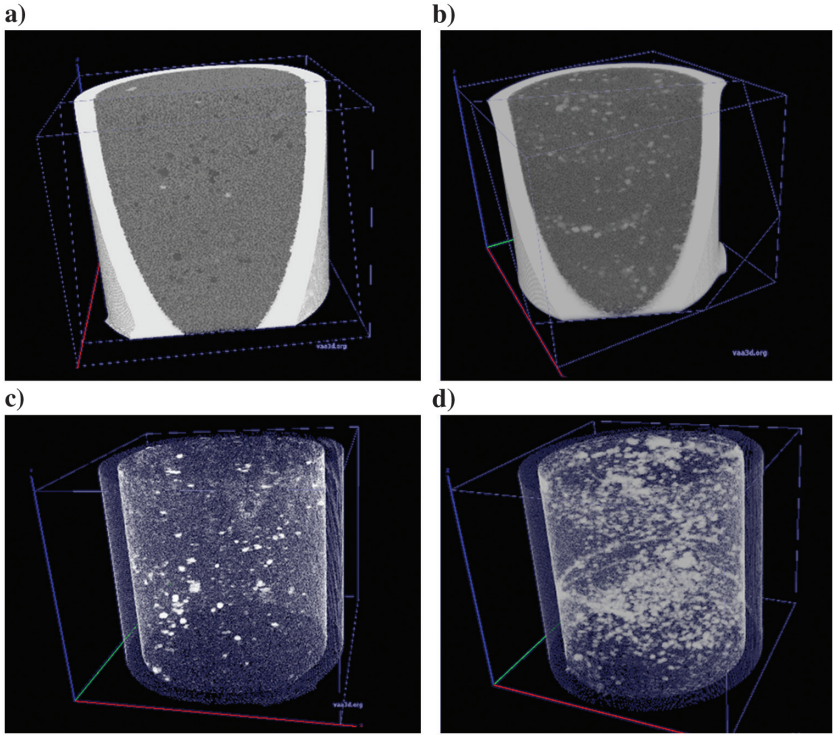

Figure 7. (a) Three-dimensional visualizations created from the segmented image stack of sample PCE1 and (b) sample PCE2 (supplementary videos can be accessed through the following links: S2 and S3). (c) Transparent 3D view showing the distribution of the PCE phase in sample PCE1 and (d) sample PCE2 (supplementary videos can be accessed through the following links: S4 and S5).

Table 2. Actual sample properties as obtained by X-ray tomography and image analysis.

	Clean	PCE1	PCE2
Porosity(%)	37	44	40
Water content (%)	37	41	35
PCE (% of pore space)	—	1.5	11
Air (% of pore space)	—	4.4	1.2
Water (% of pore space)	—	94.1	87.8

The image calculations also enabled a quantification of the amount and volumes of the PCE blobs in each sample. The blob volume distribution can be used as a qualitative measure of how interconnected the PCE phase is in the respective samples. Results from both samples are shown in Figure 8. In sample PCE1, all approximately 83,000 segmented blobs have volumes below approximately 1 mm^3. The three largest blobs have volumes of 1.1, 1.0, and 0.7 mm^3, corresponding to 3%, 3%, and 2% of the total PCE volume in the sample. These numbers indicate that the PCE phase is mainly distributed as isolated blobs with relatively well-distributed volumes of <1 mm^3.

In contrast to the well-distributed pattern of blob volumes in PCE1, sample PCE2 contained five major PCE blobs that stand out in Figure 8 in comparison with the rest of the approximately 152,000 smaller blobs. The largest of the major blobs has a volume of 142 mm^3, which corresponds to 31% of the total amount of PCE in the sample. The second and third largest blobs have volumes of 38 and 11 mm^3, respectively, corresponding to 8% and 2% of the total PCE amount. It is evident that these larger blobs must be interconnected across several grains and pores, an observation also indicated by visual analysis.

The average volume of grains in the two samples is 0.018 mm^3 (shown with a vertical line in Figure 8), and 98% of the grains have volumes less than 0.04 mm^3. According to these calculations, approximately 92% of the PCE blobs are larger than the mean grain size in sample PCE2. The corresponding number for the PCE1 sample is 60%.

SIP results

Figure 9a shows the results from a test SIP measurement on the NaCl electrolyte together with the theoretical response of the electrolyte calculated from equation 3. The measured and calculated data are in acceptable agreement with each other over the entire frequency range. The error bars of the data points are of the same order of magnitude as the markers, except for occasional data points appearing as outliers with high standard deviation values (the mean standard deviation of the phase data is 0.06 and 0.02 mrad in Figure 9a and 9b, respectively). The reason for the presence of these outliers is not clear (except when they appear at the power grid frequency of 50 Hz as in Figure 9b), but they are likely due to stochastic electromagnetic noise.

In Figure 9b, the imaginary part of the SIP signal measured on the clean sample is plotted together with a replica sample in which the same sand and electrolyte was used. The comparison in Figure 9b shows that the sample preparation method is repeatable and yields similar bulk properties for water-saturated sand samples.

The results from the SIP measurements on the clean sand sample and the PCE-contaminated samples, PCE1 and PCE2 (before the X-ray tomography scanning), are shown in Figure 10. The results in Figure 10a show that the real conductivity is increased slightly in sample PCE1 and more pronounced in PCE2, compared with the clean sample. Simultaneously, the imaginary part of the complex

conductivity (Figure 10b) decreased relative to the clean sand sample in PCE1 and PCE2. Although the difference is small, the imaginary part decreased more in PCE2 than in PCE1 for frequencies lower than 30 Hz. Figure 10c shows the phase responses of the samples, which are very similar to the imaginary part response in Figure 10b. This means that the phase spectra are not mainly determined by the differences in real conductivity observed in Figure 10a.

The shapes of the phase and imaginary conductivity spectra in Figure 10b and 10c resemble a Cole-Cole model at low frequencies (<1 Hz). The phase data in Figure 10c are fitted with double Cole-Cole models. The fitted models are shown with solid lines, and the corresponding Cole-Cole parameters of the relaxations for each sample are reported in Table 3. According to the fitted parameters, the low-frequency relaxation time shifts to slightly different values in the PCE-contaminated samples compared with the clean sand sample (from 1.69 s for the clean sand to 1.92 s for PCE1 and 1.37 s for PCE2).

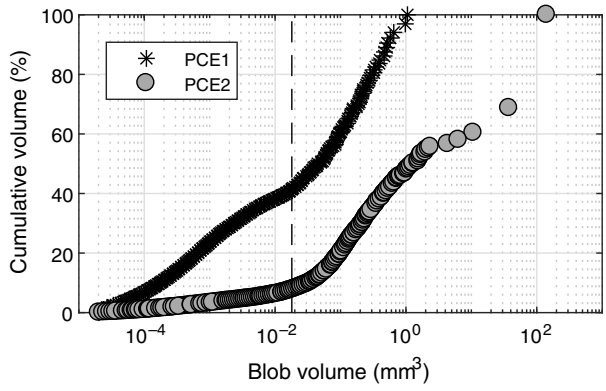

Figure 8. Size distribution of the PCE blobs in the samples. The vertical dashed line represents the average volume of the grains in the samples.

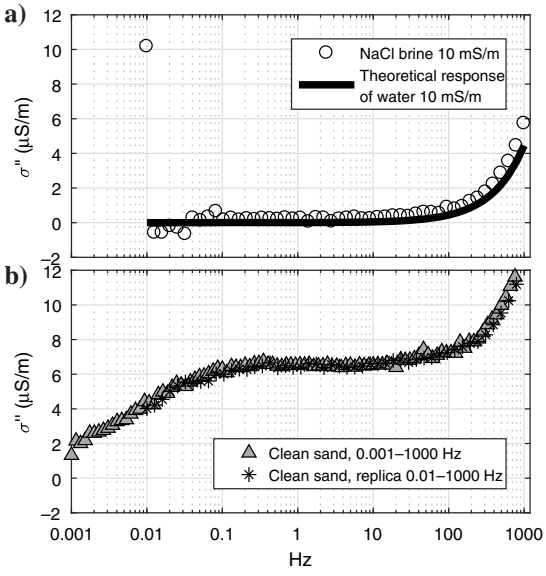

Figure 9. (a) Results from test measurement on 10 mS/m NaCl electrolyte showing an acceptable agreement with the calculated theoretical response of the electrolyte. (b) Repeated measurements on the same type of sand and electrolyte show repeatability in the SIP results.

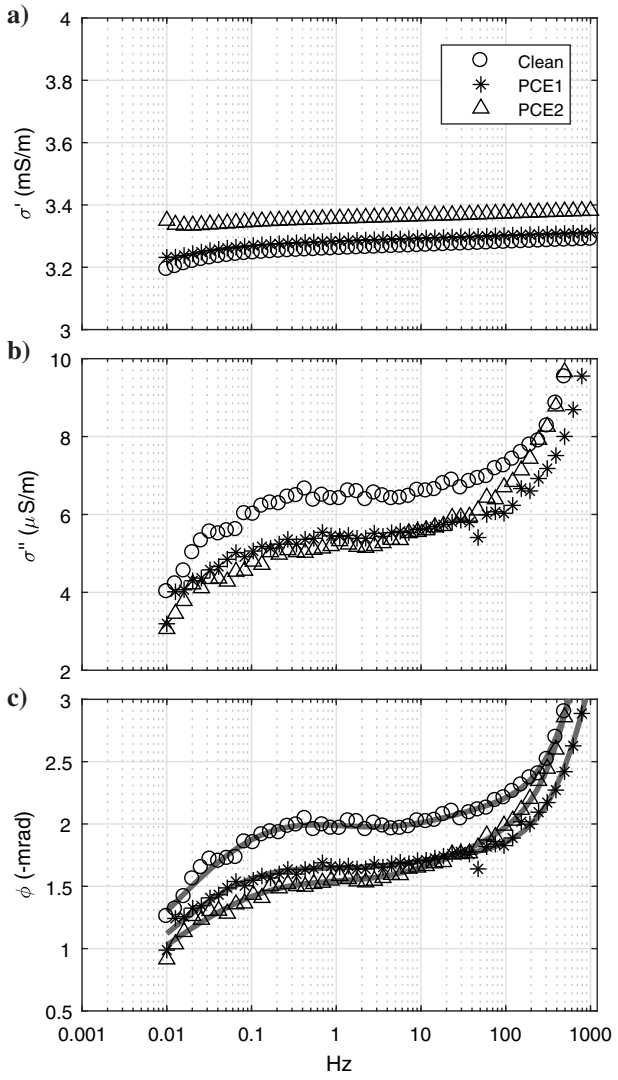

Figure 10. Results of SIP measurements on the clean sand sample and the contaminated samples PCE1 and PCE2. (a) The real conductivity is generally higher in the contaminated samples compared with the clean sample, whereas (b) the imaginary conductivity is generally lower. (c) The phase spectra follow the same pattern as the imaginary conductivity. Here, the phase data are fitted with a triple Cole-Cole model to extract the Cole-Cole parameters of the low-frequency response.

Table 3. Cole-Cole parameters of the low- and high-frequency relaxations in the fitted models shown in Figure 10c.

	Low frequency			High frequency		
	m_0 (mV/V)	τ (s)	c	m_0 (mV/V)	τ (s)	c
Clean	8.1	1.69	0.30	57	9.8×10^{-7}	0.45
PCE1	6.8	1.92	0.30	60	4.4×10^{-7}	0.43
PCE2	6.6	1.37	0.30	73	1.3×10^{-6}	0.50

Between 1 and 100 Hz, the spectra in Figure 10b and 10c flatten out before a steep increase above approximately 100 Hz. The steepness of the increase between 100 and 1000 Hz is largest for sample PCE2. SIP data at frequencies above 100 Hz are usually attributed to Maxwell-Wagner effects (e.g., Loewer et al., 2017) and/or inductive coupling effects. Our control measurements on electrolyte (Figure 9a) indicate only small errors due to coupling effects at these frequencies, leaving the permittivity of water as the main source to the increase in imaginary conductivity observed above 100 Hz in Figure 9a.

To evaluate the importance of dielectric permittivity on the imaginary conductivity spectra measured on the clean and contaminated sand samples, we used the models presented in Sen et al. (1981) and Brovelli and Cassiani (2010) together with the sample properties obtained from the image analysis to calculate bulk permittivities. The results are presented in Figure 11 (note the different scales compared with Figure 10), in which the imaginary conductivity has been calculated from the bulk permittivities according to equation 3. In Figure 11a, Archie's cementation exponent m is calibrated so that the calculated real conductivity with 37% porosity fits the real conductivity values measured on the clean sand sample (see Figure 10a). Relative to a water-saturated sand with 37% porosity, Figure 11a shows that the real conductivity is expected to decrease

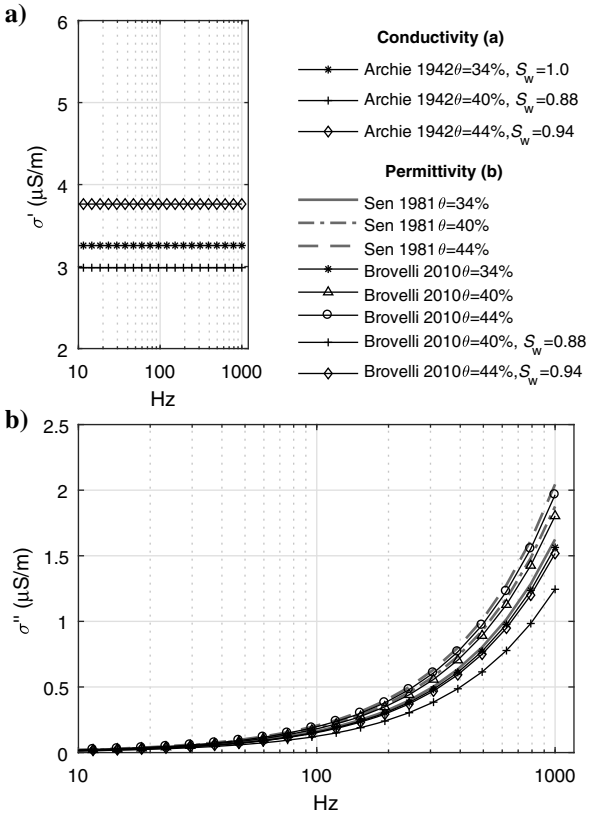

Figure 11. (a) DC conductivity for samples with different porosity and water saturation according to Archie's law (Archie, 1942). The water conductivity is 10 mS/m, and Archie's cementation exponent is fixed at 1.12. For the unsaturated samples, Archie's saturation exponent is 2. (b) Theoretical response of the imaginary conductivity (equation 4) for various two- and three-phase mixtures according to the permittivity models of Sen et al. (1981) and Brovelli and Cassiani (2010).

in a sand with 40% porosity and 88% water saturation (representing sample PCE2). However, in our measurements, the opposite result was obtained; larger real conductivity values were measured on sample PCE2 compared with the clean sample. Figure 11a also shows that the real conductivity according to Archie's law is expected to increase significantly in the sand with 44% porosity and 94% water saturation (representing sample PCE1) relative to the water-saturated sand with 37% porosity. The results in Figure 10a show that the real conductivity only increased slightly in sample PCE1 relative to the clean sand.

Figure 11b shows the theoretical influence of the sample permittivity on the imaginary conductivity values between 10 and 1000 Hz. The low-frequency approximation of the Bruggeman-Hanai-Sen equation is valid for mixtures under the conditions that $\sigma_w \gg \omega(\varepsilon'_w - \varepsilon'_g)$ and $\sigma \gg \omega(\varepsilon' - \varepsilon'_g)$, where σ and σ_w are the conductivity values of the mixture and water, respectively, whereas ε', ε'_w, and ε'_g are the real permittivity values of the mixture, water, and grains, respectively (Sen et al., 1981). For the mixtures plotted in Figure 11b, σ and σ_w are more than 1000 times larger than the right sides of the inequalities at 1000 Hz, which justifies the use of the low-frequency approximation of the Bruggeman-Hanai-Sen equation. The models from Sen et al. (1981) and Brovelli and Cassiani (2010) give consistent predictions of the sample permittivity for water-saturated sands with porosities of 37%, 40%, and 44%, respectively. According to the results in Figure 11b, the imaginary conductivity is expected to be slightly less influenced by the dielectric permittivity in three-phase systems (representing samples PCE1 and PCE2) compared with purely water-saturated sands. Comparing Figure 11b with the measured imaginary conductivity data in Figure 10b, it is evident that the dielectric permittivity of the samples alone cannot explain the steep increase in the data between 10 and 1000 Hz. Samples PCE1 and PCE2 seem to increase more than the clean sample in this frequency range, which is in contradiction to the calculated responses in Figure 11b.

SIP measurements repeated over time

SIP measurements were performed before and after the X-ray tomography. During the preparation of the PCE1 sample, a replica was prepared from the same sand-PCE mixture in a second sample holder. Figure 12a–12c shows results of all SIP measurements performed on sample PCE1 and on the replica. The results differ slightly between the two samples immediately after packing (day 1, 12:00 in Figure 12a–12c). One main reason for this is probably that the phase data are more noisy at the low-frequency end of the replica sample (as indicated by the scattered appearance of the data in Figure 12b and 12c and the size of the mean standard deviation values of the first data five data points, 0.15 mrad). If these data points would be excluded, the imaginary part spectrum (Figure 12b) would be close to identical as the spectrum from the PCE1 sample. However, after being left standing for 20 h, the measured real and imaginary conductivity as well as the phase spectra of the replica sample (day 2, 8:00 in Figure 12a–12c) are almost identical to the spectra measured on the scanned sample PCE1 directly after packing (day 1, 12:00). The standard deviation values of the low-frequency data also decreased to acceptable values (0.05 mrad). Therefore, it is likely that it took a few hours to reach an electrochemical equilibrium in the replica sample, in contrast to the PCE1 sample.

The results of the SIP measurements on the scanned sample PCE1 after the X-ray tomography (Day 2, 15:00 in Figure 12a–12c) show that the real part of the conductivity increased after the scanning. The relative magnitudes of the phase results are no longer similar to the relative magnitudes of the imaginary conductivity spectra, indicating that the phase data (Figure 12c) are influenced by the increase in real conductivity. The shape of the imaginary conductivity (Figure 12b) changed after the scanning and decreased at frequencies below approximately 2 Hz and above approximately 200 Hz, whereas it increased slightly at frequencies between approximately 2 and 200 Hz.

For practical reasons, no replica sample was packed when PCE2 was prepared. Figure 12d–12f shows the results of the SIP measurements before and after the X-ray tomography scanning of PCE2. Similar patterns, such as for sample PCE1 (Figure 12a–12c), can be observed in Figure 12d–12f; the real conductivity increases (Figure 12d), and the shape of the imaginary conductivity spectrum changes (Figure 12e) after the scanning, whereas the phase spectrum (Figure 12f) is affected by the combination of these changes. The imaginary conductivity decreases after the scanning at low frequencies (in this case below approximately 0.5 Hz), similar to PCE1. In contrast to PCE1, the imaginary conductivity increased in PCE2 at frequencies greater than 1 Hz.

A different behavior compared to the contaminated samples can be seen for the clean sand sample (Figure 12g–12i). The first SIP spectrum was collected shortly after the sample preparation, and the second measurement was performed approximately 15 h later. During this time, no significant differences can be found in the SIP results. The third measurement was carried out directly after the X-ray tomography. Even though the time period between the second and third measurement is shorter (approximately 9 h), the real conductivity has now increased significantly (Figure 12g). However, in contrast to the contaminated samples, no significant change of the imaginary conductivity spectra can be observed after the X-ray tomography (Figure 12h). The decrease of the phase response (Figure 12i) can be explained by the increase of the real conductivity (Figure 12g).

DISCUSSION

The effect of NAPLs on the low-frequency SIP response

The membrane and electrochemical polarization mechanisms (described briefly in the theory section) are clearly dependent on the geometric arrangements of grains and pores in the geologic material. Different alterations of the pore space geometry due to the presence of NAPLs were discussed by Johansson et al. (2015) in light of both polarization mechanisms. In this section, we will discuss the actual NAPL configurations obtained in our samples and interpret the measured change in SIP results. For brevity, we refer the reader to Johansson et al. (2015) for more details on the theoretical relationships between NAPL geometry and the membrane or electrochemical polarization mechanisms.

The SIP results from our study show that the real conductivity of the samples was high in the PCE-contaminated sand samples compared with the clean sand. This result is in contradiction to many previous studies in which the displacement of water by high-resistive NAPLs have resulted in decreased conductivity of the sample (e.g., Chambers et al., 2004; Cassiani et al., 2009; Schmutz et al., 2012; Ustra et al., 2012). However, increased real conductivity with

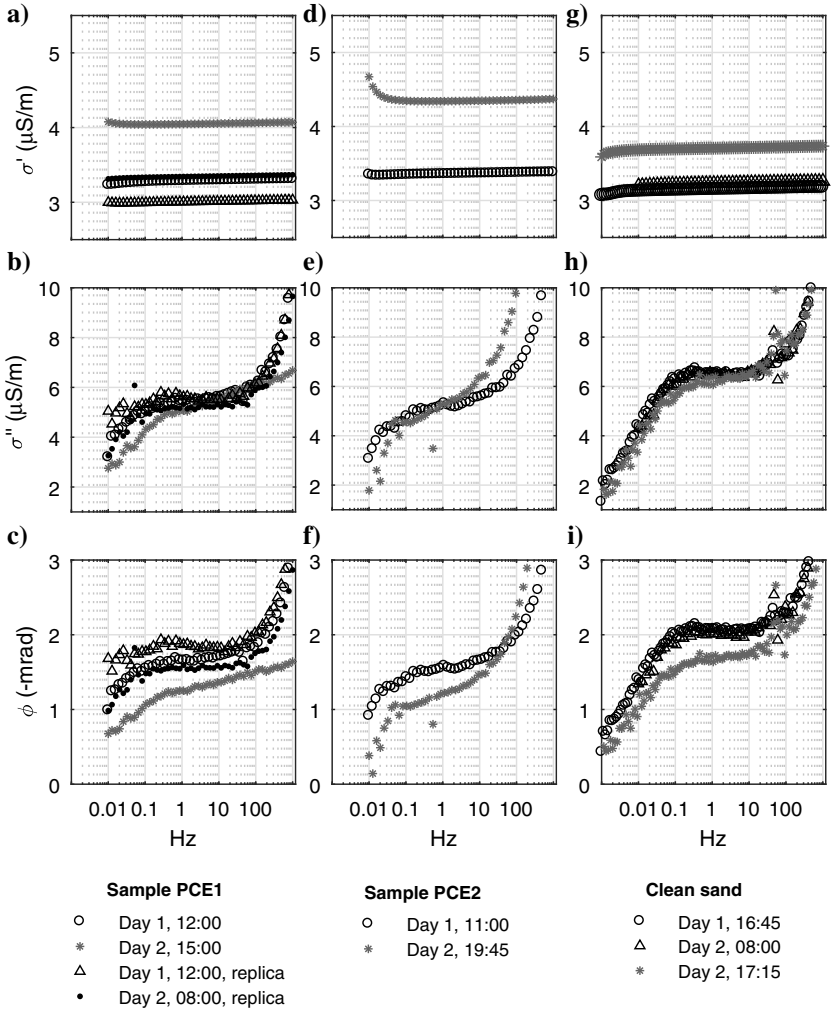

Figure 12. Results from measurements repeated over time for samples (a-c) PCE1, (d-f) PCE2, and (g-i) the clean sand. (a) The real part increases after the X-ray scanning in PCE1, and (b) the imaginary part decreases at frequencies less than approximately 2 Hz and above approximately 200 Hz, whereas it increases slightly between approximately 2 and 200 Hz. (c) The phase spectrum in PCE1 is affected by the increase in real conductivity. (d) The real part increases after the X-ray scanning in PCE2, and (e) the imaginary part decreases at frequencies less than approximately 0.5 Hz and increases greater than approximately 1 Hz. (f) The phase spectrum in PCE2 is affected by the increase in real conductivity. (g) The real part increased significantly in the clean sand sample after the X-ray tomography around noon on day 2. (h) The imaginary part spectrum did not change significantly with time or by exposure to X-rays. (i) The phase data decreased in the clean sand sample after the X-ray tomography as a result of the increased real conductivity.

increasing NAPL content has also been observed in previous laboratory studies (e.g., Revil et al., 2011). In this previous work, the increasing conductivity in samples contaminated with oil under oil-wet conditions is attributed to an increased presence of polar components at the water-oil interface. In addition, Schwartz et al. (2012) and Shefer et al. (2013) observe increased the real conductivity in unsaturated samples contaminated with diesel fuel or motor oil and decane, respectively. Schwartz et al. (2012) interpret the increased real conductivity as an effect of an exchange process between polar organic compounds and inorganic cations in the EDLs of the soil grains. This would lead to a release of inorganic cations to the water (which was confirmed by conductivity measurements on water extracted from the samples) and, thus, an increase in the bulk conductivity.

In contrast to the light NAPL species used in the studies by Revil et al. (2011), Schwartz et al. (2012), and Shefer et al. (2013), PCE is a nonpolar chemical compound. The presence of polar organic compounds bound at the mineral or oil surfaces can therefore not be expected in our samples shortly after the sample preparation. The SIP results and image analysis on sample PCE2 also rule out the possibility that the increased real conductivity measured in this sample is purely an effect of different bulk properties (see Figures 10a and 11a). Instead, we believe that EDLs form around the nonpolar DNAPL phase due to negatively charged interfaces between nonpolar oil and water (see the discussion in Johansson et al., 2015). This hypothesis is supported by measured negative zeta potentials associated with other nonpolar oils (Marinova et al., 1996). The increased real conductivity observed for sample PCE2 in our study can be interpreted as increased surface conductivity due to the interconnected surfaces of the PCE phase and the sand grains. The X-ray tomography and the image analysis show that the PCE blobs are larger than the sand grains and that the grains are often encapsulated or bridged by the PCE. Assuming that EDLs form around the PCE phase, the presence of PCE in the pore space probably enhances current transport through the sample by providing straighter (and possibly stronger) surface conduction paths than would exist in a clean sand sample. Recent modeling results by Bücker et al. (2017) support the nonintuitive interpretation of increased sample conductivity due to surface conduction along NAPLs. With high NAPL zeta potential, their modeling results show that the high ion concentrations in the EDL of the NAPL droplets seem to reverse the insulating effect of the NAPL phase displacing electrolyte (Bücker et al., 2017).

Surface conduction along interconnected EDLs of the PCE phase could also explain the decreased imaginary conductivity in sample PCE2, as previously discussed for conceptual model C in Johansson et al. (2015). The electrochemical polarization mechanism is based on the assumption that the fixed layer around the sand grains is discontinuous and therefore contributes to the polarization. For an interconnected PCE phase, the fixed layer of the EDL would also be interconnected and therefore not contribute to any polarization. Like the assumed interconnected nature of the diffuse layer in mechanistic models (Leroy et al., 2008; Revil and Florsch, 2010), this geometry would only contribute to surface conduction. Similar conclusions can be drawn if the membrane polarization mechanism is considered. Because this mechanism considers the diffusion of ions along alternating series of different ion transparency in the pore space, occupation of the pore space with an interconnected PCE phase would theoretically block the mechanism (Johansson et al., 2015) and/or occupy the nonselective zones (i.e., the pores). Occupation of nonselective zones could disable the necessary alternating geometry for the membrane polarization mechanism.

The NAPL configuration obtained in this study for sample PCE2 resembles a combination of conceptual models C and D in Johansson et al. (2015), i.e., a continuous NAPL phase through several pores (C) and NAPL phase coating grains (D). For both conceptual models, a decrease in the polarization magnitude is expected when the electrochemical polarization mechanism is considered. For model D, it is the larger particle sizes of the PCE-coated grains that might result in the lower net polarization of the sample (however, this prediction also depends on the relative EDL strengths of grains and NAPLs and might only be valid if the EDL of the PCE is weaker than the grain EDL; see Johansson et al., 2015).

The electrochemical polarization mechanism also predicts increased relaxation times for conceptual model D (due to the larger particle sizes), whereas no change in relaxation time is expected for model C (due to the unaltered dominant length scales in the sample; see Johansson et al., 2015). This is in contradiction to our data, assuming that the relaxation time values obtained from the Cole-Cole model fitting of PCE2 and the clean sand sample (Table 2) are significant. In contrast, a decrease in the relaxation time for conceptual model D can be predicted from the membrane polarization mechanism (due to the reduced length scale of the nonselective pores; see Johansson et al., 2015), whereas this mechanism was expected to be absent for model C by Johansson et al. (2015) as discussed above. The change in relaxation time in the current study is thus in agreement with conceptual models C and D in Johansson et al. (2015) if it is assumed that the spectral responses of the NAPL-contaminated samples are mainly determined by the membrane polarization mechanism. According to the recent modeling of the membrane polarization mechanism from Bücker et al. (2017), a decrease in membrane polarization can be expected at higher NAPL concentrations after an initial increase. A possible existence of a critical snap-off value might explain why the results in this study show a decrease of polarization magnitude, whereas in Johansson et al. (2015) an increase for model D is predicted for the membrane polarization mechanism. However, the observed decrease in polarization magnitude in our study might also indicate an influence of the electrochemical polarization mechanism overlapping the membrane polarization response. The predicted increase in membrane polarization magnitude due to conceptual model D might, for example, be overridden by a decrease in the electrochemical polarization magnitude due to conceptual model C.

For sample PCE1, the higher porosity, compared with the clean sand, is probably a major reason for the observed increase in real conductivity. The image analysis showed that the porosity of sample PCE1 is significantly larger than expected (Tables 1 and 2). The measured increase in the bulk conductivity of sample PCE1, relative to the clean sample, is however significantly lower than the value estimated with Archie's law (Figures 10a and 11a). This suggests that there might be other mechanisms active in the sample that prohibit the current transport.

The X-ray tomography images reveal that the PCE1 sample contained more air bubbles compared to the PCE2 sample. The presence of air bubbles should theoretically have the effect of increasing the imaginary conductivity by strengthening the current path through the EDLs (Titov et al., 2004; Cassiani et al., 2009).

Research has also confirmed the existence of a negative zeta potential of gas bubbles in water (Yang et al., 2001), which theoretically could increase the total electrochemical polarization of the sample due to air bubble-associated EDLs. However, the opposite result is observed in this study. It is probable that the size of the air voids play an important role; although air voids in desaturated samples are of smaller size than the pores (as in the samples in Titov et al., 2004), the size of the air bubbles in our samples (trapped during the mixing of moist sand and PCE) is often large. Air bubbles larger than the pores will not force current transport through the EDLs of all the grains like the presence of air will when the current path is intact, i.e., when water drains from the pores but remains in the pore throats and as water films around the grains. Other possible explanations for the decrease in the imaginary conductivity of sample PCE1 might be the relatively large porosity and/or the fact that 60% of the PCE blobs in the sample have larger volumes (and thus smaller specific surface areas) than the average grain volume of the sand.

Our results indicate that the Cole-Cole relaxation times increased in PCE1 compared with the clean sand, indicating longer characteristic length scales in the DNAPL-contaminated sample. A possible explanation might be that the PCE blobs increase the average particle size in the samples, a mechanism discussed by Johansson et al. (2015). Increased relaxation times in NAPL-contaminated samples were observed also by Cassiani et al. (2009), Schmutz et al. (2010), and Revil et al. (2011). It is possible that in their experiments, the NAPL phase was also configured in blobs larger than the average grain size.

The sample PCE1 in this study does not directly resemble any of the conceptual models in Johansson et al. (2015), although several grains were occasionally coated with NAPLs, similar to conceptual model D. The changing SIP results from PCE1, relative to the clean sand sample, are probably caused not only by the distribution of PCE blobs. The X-ray tomography and image analysis revealed that the differences in the SIP signals more likely are caused by a combination of the higher water content, a significant amount of large air bubbles, and large PCE blobs. All of these factors can be expected to decrease the polarization magnitude of the sample.

High-frequency SIP response

SIP data at frequencies below approximately 10 Hz measured on metal-free soils are often discussed in terms of the electrochemical and/or membrane polarization mechanisms. Interpretations in terms of these low-frequency mechanisms are generally accepted in the research field, whereas it is more uncommon in the literature with comprehensive analyses of the frequency range approximately 10–1000 Hz and above. In several studies, SIP data at frequencies greater than 10–100 Hz are attributed to the Maxwell-Wagner effect and/or coupling effects (e.g., Revil and Florsch, 2010; Weller et al., 2010; Zisser et al., 2010; Loewer et al., 2017). According to a relatively recent review of the SIP method (Kemna et al., 2012), the Maxwell-Wagner polarization mechanism is mainly relevant above 1 kHz.

The Maxwell-Wagner effect is an electric relaxation that occurs in composite materials due to conductivity and permittivity differences in the medium. The Bruggeman-Hanai-Sen effective medium equation is frequently used to model the Maxwell-Wagner effect in granular media (Sen et al., 1981). In this study, we used the low-frequency approximation of the Bruggeman-Hanai-Sen equation to calculate the dielectric permittivity of our samples (Figure 11b), thereby assuming that the Maxwell-Wagner relaxation occurs at frequencies higher than our measurement range. At frequencies above the Maxwell-Wagner relaxation, the real part of the permittivity decreases, which is equivalent to a decrease in the imaginary part of the conductivity.

Although the dielectric permittivity can explain the high-frequency increase in the imaginary conductivity of water samples (Figure 9a), the magnitudes calculated with mixing models in this study is not sufficient to explain the observed high-frequency SIP behavior (Figures 10b and 11b). According to Sen (1981), remarkably high values of dielectric permittivity can be observed in geologic materials. These values greatly exceed the permittivity values of the mixture components, and the phenomenon can be explained theoretically by certain geometric factors in the samples. Such geometric factors are, for example, the presence of so-called dead-end pores with encapsulated water or small concentrations of high-aspect-ratio particles in the sample (Sen, 1981). In our data, it is possible that the steep increase in imaginary conductivity in sample PCE2 is related to such geometric effects. However, more research is needed to verify this hypothesis.

An alternative explanation, to the one given above, of the large values of imaginary conductivity at higher frequencies, is that they are caused by polarization of ions at the particle surfaces in the sample. In previous research, several models have been developed in which analytical descriptions of the electrochemical and/or membrane polarization are combined with macroscopic mixing models (often the Bruggeman-Hanai-Sen equation). Examples of such models are presented by de Lima and Sharma (1992), Leroy et al. (2008), and Kremer et al. (2016). However, the use of most of these models requires detailed knowledge about appropriate values for a range of parameters describing the EDLs in the samples. This kind of information cannot be obtained from the current experiment. Future research about the SIP response of NAPL-contaminated samples should therefore focus on the EDL properties of the NAPLs of interest.

X-ray interactions and changed SIP response

The SIP measurements performed after the X-ray tomography indicated that changes occurred during the scanning of all samples. Redistribution of the grain or NAPL phases can be excluded as a reason because the tomography results showed no sign of sample movement during the approximately 4 h scans. The data from the clean sand sample suggest that the salinity of the water increased due to interactions with the X-rays. Because no significant increase in real conductivity occurred during the approximately 15 h long time period between the first two measurements, it is unlikely that any electrochemical evolution during the approximately 9 h long time period between the second and third measurement is the cause of the increase in real conductivity. A more likely explanation is that the X-ray interactions with the materials changed the samples enough for the results to be measureable with SIP. At energies below the 160 kV used here, the X-ray attenuation is caused by the photoelectric effect and Compton scattering processes, both of which involve ejection of electrons from the studied materials. It is well-known that X-ray interaction with water leads to ionization and excitation of water molecules as well as hydrated electrons (water radiolysis). This interaction is quickly followed by different chemical reactions with water molecules, resulting in ionic products (OH^- and H_3O^+), radicals (H, OH, and H_2O), and molecular

products (H_2 and H_2O_2). The ions and radicals also react with other materials, e.g., oxides such as SiO_2 and dissolved metals (Le Caër, 2011). Electrical conductivity has been used as a tool to study water radiolysis (Le Caër, 2011), and an irreversible increase in electrical conductivity after X-ray irradiation of water has been observed (Schmidt, 1960).

The real conductivity also increased significantly in the contaminated samples PCE1 and PCE2 after the X-ray tomography scanning. For unknown reasons, the real conductivity increased more at low frequencies (<0.05 Hz) than at higher frequencies, especially in PCE2 (Figure 12d). In contrast to the clean sand sample, the shapes of the imaginary part spectra also changed after the X-ray tomography. This indicates that the X-rays could also have changed the chemical properties of the PCE fluid. Elsewhere, controlled PCE radiolysis experiments have resulted in chemical degradation and acidic products (Sutherland and Spinks, 1959). Another possible reason for the changing SIP results might be that the electrochemical environment in the samples changes or stabilizes with time, as has been observed in other studies of NAPL-contaminated samples (e.g., Olhoeft, 1985; Shefer et al., 2013). However, it is interesting to observe different behaviors of sample PCE1 after the X-ray scanning and the replica that was left in the laboratory. The real and imaginary conductivity had changed more significantly in sample PCE1 after 27 h compared with the changes in the replica sample after 20 h. In sample PCE2, significant changes could be observed after only 9 h. A possible reason for the increased rate of change in the scanned samples might be the elevated temperature in the tomograph. The temperature is fixed at 28°C, and the total scan time for each sample was approximately 4 h. In addition, the X-ray beam might cause further local heating of the samples, although this effect is probably very small.

Possible reasons for the change in spectral shape of the real and imaginary conductivity in PCE1 and PCE2 after the tomography remain unknown. The imaginary conductivity results, however, indicate some changes in the chemical or physical properties of the interfaces in the samples, which are not visible at the micrometer scale.

A discussion on sample preparation

The sample preparation method used in this experiment is similar to the methods described in several previous studies (Martinho et al., 2006; Schmutz et al., 2010, 2012; Revil et al., 2011; Schwartz et al., 2012; Ustra et al., 2012; Shefer et al., 2013). In all of these studies, the sample preparation method is based on manual mixing of the sample constituents before the columns were packed. The geometric NAPL configurations A and B (of Johansson et al., 2015), i.e., small NAPL droplets isolated in the pores or pore throats of the sample, could not be obtained in this experiment with this preparation method. The sample preparation method itself probably limits the possibilities of obtaining different geometric distributions of the PCE phase in the samples. Therefore, it is important to also use other sample preparation methods in similar future studies, e.g., with volumetric injection of PCE into a packed sand sample as used by Cassiani et al. (2009). To obtain more realistic and field-like PCE configurations in the samples, another approach would be to let the dense PCE fluid sink through a packed and water-saturated sand sample. Although these kinds of sample preparations are practically difficult to fulfill due to the chemical aggressiveness of PCE, they might result in geometric PCE configurations different to those obtained in the current experiment, e.g., configurations more similar to conceptual models A and B in Johansson et al. (2015).

The combination of SIP measurements and X-ray tomography scanning of the same samples in this study gives important insights into what samples properties are actually achieved with the given sample preparation method. The concentration of PCE in the scanned part of the packed sample holders is significantly lower than expected when the sand-PCE mixtures were prepared. It is likely that other experiments of this kind in previous research also yielded sample properties different from the targeted ones. The combination of SIP with high-resolution X-ray tomography is, therefore, an important tool for future experimental investigations of the SIP response of NAPL-contaminated samples as demonstrated in this study.

CONCLUSION

In this study, three samples with increasing concentration of PCE have been tested for SIP response and scanned with high-resolution X-ray tomography. We interpret the relative decrease of the SIP phase and imaginary conductivity in PCE-contaminated samples as a combination of two effects. The first effect is a result of interconnected grain EDLs, caused by surface conductivity along the PCE phase. The second effect is a result of groups of grains coated in PCE, in which the PCE prohibits the EDLs around these grains and decreases the specific surface area in the sample.

NAPL configurations characterized by presence of small NAPL droplets in pores or pore spaces could not be obtained with the sample preparation method used in this study. To investigate the SIP response of these NAPL geometries further, a different sample preparation method is recommended. However, the practical issues encountered when an aggressive chemical such as PCE is used in laboratory would probably be increasingly difficult to handle with different sample preparation methods.

We conclude that the combination of SIP measurements with high-resolution X-ray tomography and image analysis on the same samples is a highly useful approach. Our results show that the real sample properties (mainly the distribution of the contaminant phase) differ from the expected result despite careful sample preparation. In addition to the possibility of quantifying many sample properties relevant for the low-frequency behavior of SIP, X-ray tomography can, in future studies, also be used for detailed analysis of the effects of the geometry at microscale on the sample permittivity. With such studies, the SIP behavior of different samples at frequencies above 10–1000 Hz might be better understood and interpreted.

ACKNOWLEDGMENTS

We would like to acknowledge E. Zimmermann and S. Huisman for instrument support and expert advice on sample holder design as well as G. Cassiani for cooperation and access to the ZWL-SIP04 impedance meter. Many thanks also to L. Slater and three anonymous reviewers for helping us to improve this paper. Funding that made this work possible was provided by BeFo, Swedish Rock Engineering Research Foundation (ref. 331) and SBUF, The Development Fund of the Swedish Construction Industry (ref. 12719 and 13232), Formas, The Swedish Research Council for Environment, Agricultural Sciences and Spatial Planning, provided funding for this presentation of the results (ref. 2012-1931) as part of the

Geoinfra-TRUST framework (http://www.trust-geoinfra.se/), Sven Tyréns Stiftelse and Innovation Fund Denmark.

DATA AND MATERIALS AVAILABILITY

Data associated with this research are available and can be obtained by contacting the corresponding author.

REFERENCES

Ajo-Franklin, J. B., J. T. Geller, and J. M. Harris, 2006, A survey of the geophysical properties of chlorinated DNAPLs: Journal of Applied Geophysics, **59**, 177–189, doi: 10.1016/j.jappgeo.2005.10.002.

Al-Raoush, R. I., and C. S. Willson, 2005, A pore-scale investigation of a multiphase porous media system: Journal of Contaminant Hydrology, **77**, 67–89, doi: 10.1016/j.jconhyd.2004.12.001.

Archie, G. E., 1942, The electrical resistivity log as an aid in determining some reservoir characteristics: Transactions of the American Institute of Mining, Metallurgical, and Petroleum Engineers, **146**, 54–62.

Berger, M. J., J. H. Hubbell, S. M. Seltzer, J. Chang, J. S. Coursey, R. Sukumar, D. S. Zucker, and K. Olsen, 2010, XCOM: Photon cross section database (version 1.5): National Institute of Standards and Technology, http://physics.nist.gov/xcom, accessed 5 February 2018.

Börner, F., M. Gruhne, and J. Schön, 1993, Contamination indications derived from electrical properties in the low frequency range: Geophysical Prospecting, **41**, 83–98, doi: 10.1111/j.1365-2478.1993.tb00566.x.

Brovelli, A., and G. Cassiani, 2010, A combination of the Hashin-Shtrikman bounds aimed at modelling electrical conductivity and permittivity of variably saturated porous media: Geophysical Journal International, **180**, 225–237, doi: 10.1111/j.1365-246x.2009.04415.x.

Brusseau, M. L., H. Janousek, A. Murao, and G. Schnaar, 2008, Synchrotron X-ray microtomography and interfacial partitioning tracer test measurements of NAPL-water interfacial areas: Water Resources Research, **44**, 1–9, doi: 10.1029/2006WR005517.

Bücker, M., A. Flores Orozco, A. Hördt, and A. Kemna, 2017, An analytical membrane-polarization model to predict the complex conductivity signature of immiscible liquid hydrocarbon contaminants: Near Surface Geophysics, **15**, 547–562.

Bücker, M., and A. Hördt, 2013, Long and short narrow pore models for membrane polarization: Geophysics, **78**, no. 6, E299–E314, doi: 10.1190/geo2012-0548.1.

Cassiani, G., A. Kemna, A. Villa, and E. Zimmermann, 2009, Spectral induced polarization for the characterization of free-phase hydrocarbon contamination of sediments with low clay content: Near Surface Geophysics, **7**, 547–562, doi: 10.3997/1873-0604.2009028.

Chambers, J. E., M. H. Loke, R. D. Ogilvy, and P. I. Meldrum, 2004, Noninvasive monitoring of DNAPL migration through a saturated porous medium using electrical impedance tomography: Journal of Contaminant Hydrology, **68**, 1–22, doi: 10.1016/S0169-7722(03)00142-6.

Cnudde, V., and M. N. Boone, 2013, High-resolution X-ray computed tomography in geosciences: A review of the current technology and applications: Earth-Science Reviews, **123**, 1–17, doi: 10.1016/j.earscirev.2013.04.003.

Culligan, K. A., D. Wildenschild, B. S. B. Christensen, W. G. Gray, and M. L. Rivers, 2006, Pore-scale characteristics of multiphase flow in porous media: A comparison of air-water and oil-water experiments: Advances in Water Resources, **29**, 227–238, doi: 10.1016/j.advwatres.2005.03.021.

de Lima, O. A. L., and M. M. Sharma, 1992, A generalized Maxwell-Wagner theory for membrane polarization in shaly sands: Geophysics, **57**, 431–440, doi: 10.1190/1.1443257.

Goldstein, L., S. O. Prasher, and S. Ghoshal, 2007, Three-dimensional visualization and quantification of non-aqueous phase liquid volumes in natural porous media using a medical X-ray computed tomography scanner: Journal of Contaminant Hydrology, **93**, 96–110, doi: 10.1016/j.jconhyd.2007.01.013.

Johansson, S., G. Fiandaca, and T. Dahlin, 2015, Influence of non-aqueous phase liquid configuration on induced polarization parameters: Conceptual models applied to a time-domain field case study: Journal of Applied Geophysics, **123**, 295–309, doi: 10.1016/j.jappgeo.2015.08.010.

Johansson, S., M. Rossi, and T. Dahlin, 2017b, The potential of X-ray tomography and image analysis for interpretation of spectral induced polarization measurements: 23rd European Meeting of Environmental and Engineering Geophysics, Extended Abstracts, Tu 23P1 03.

Johansson, S., E. Tudisco, M. Rossi, and S. Hall, 2017a, Interpretation of geophysical measurements using X-ray tomography of sand samples: 3rd International Conference on Tomography of Materials and Structures, Extended Abstracts.

Kemna, A., A. Binley, G. Cassiani, E. Niederleithinger, A. Revil, L. Slater, K. H. Williams, A. Flores Orosco, F.-H. Haegel, A. Hördt, S. Kruschwitz, V. Leroux, K. Tivov, and E. Zimmermann, 2012, An overview of the spectral induced polarization method for near-surface applications: Near Surface Geophysics, **10**, 453–468, doi: 10.3997/1873-0604.2012027.

Ketcham, R. A., and W. D. Carlson, 2001, Acquisition, optimization and interpretation of X-ray computed tomographic imagery: Applications to the geosciences: Computers and Geosciences, **27**, 381–400, doi: 10.1016/S0098-3004(00)00116-3.

Kremer, T., M. Schmutz, P. Leroy, P. Agrinier, and A. Maineult, 2016, Modeling the spectral induced polarization response of water-saturated sands in the intermediate frequency range (10^2–10^5Hz) using mechanistic and empirical approaches: Geophysical Journal International, **207**, 1303–1312, doi: 10.1093/gji/ggw334.

Kruschwitz, S., M. Halisch, C. Prinz, A. Weller, M. Müller-Petke, and R. Dlugosch, 2017, Towards a better understanding of electrical relaxation: Proceedings of the Annual Symposium of the Society of Core Analysts, Extended Abstracts, SCA2017–137.

Le Caër, S., 2011, Water radiolysis: Influence of oxide surfaces on H2 production under ionizing radiation: Water, **3**, 235–253, doi: 10.3390/w3010235.

Leroy, P., A. Revil, A. Kemna, P. Cosenza, and A. Ghorbani, 2008, Complex conductivity of water-saturated packs of glass beads: Journal of Colloid and Interface Science, **321**, 103–117, doi: 10.1016/j.jcis.2007.12.031.

Loewer, M., T. Günther, J. Igel, S. Kruschwitz, T. Martin, and N. Wagner, 2017, Ultra-broad-band electrical spectroscopy of soils and sediments — A combined permittivity and conductivity model: Geophysical Journal International, **210**, 1360–1373, doi: 10.1093/gji/ggx242.

Marinova, K. G., R. G. Alargova, N. D. Denkov, O. D. Velev, D. N. Petsev, I. B. Ivanov, and R. P. Borwankar, 1996, Charging of oil-water interfaces due to spontaneous adsorption of hydroxyl ions: Langmuir, **12**, 2045–2051, doi: 10.1021/la950928i.

Marshall, D. J., and T. R. Madden, 1959, Induced polarization, a study of its causes: Geophysics, **24**, 790–816, doi: 10.1190/1.1438659.

Martinho, E., F. Almeida, and M. J. Senos Matias, 2006, An experimental study of organic pollutant effects on time domain induced polarization measurements: Journal of Applied Geophysics, **60**, 27–40, doi: 10.1016/j.jappgeo.2005.11.003.

Olhoeft, G. R., 1985, Low-frequency electrical properties: Geophysics, **50**, 2492–2503, doi: 10.1190/1.1441880.

Pelton, W. H., S. H. Ward, P. G. Hallof, W. R. Sill, and P. H. Nelson, 1978, Mineral discrimination and removal of inductive coupling with multifrequency IP: Geophysics, **43**, 588–609, doi: 10.1190/1.1440839.

Poludniowski, G. G., 2007, Calculation of X-ray spectra emerging from an X-ray tube — Part 2. X-ray production and filtration in X-ray targets: Medical Physics, **34**, 2175–2186, doi: 10.1118/1.2734726.

Revil, A., and N. Florsch, 2010, Determination of permeability from spectral induced polarization in granular media: Geophysical Journal International, **181**, 1480–1498.

Revil, A., M. Schmutz, and M. L. Batzle, 2011, Influence of oil wettability upon spectral induced polarization of oil-bearing sands: Geophysics, **76**, no. 5, A31–A36, doi: 10.1190/geo2011-0006.1.

Schmidt, K., 1960, Changes in conductivity of pure water caused by x-ir-radiation: Nature, **187**, 931–932, doi: 10.1038/187931a0.

Schmutz, M., A. Blondel, and A. Revil, 2012, Saturation dependence of the quadrature conductivity of oil-bearing sands: Geophysical Research Letters, **39**, L03402, doi: 10.1029/2011GL050474.

Schmutz, M., A. Revil, P. Vaudelet, M. Batzle, P. Femenía Viñao, and D. D. Werkema, 2010, Influence of oil saturation upon spectral induced polarization of oil-bearing sands: Geophysical Journal International, **183**, 211–224, doi: 10.1111/j.1365-246X.2010.04751.x.

Schnaar, G., and M. L. Brusseau, 2006, Characterizing pore-scale dissolution of organic immiscible liquid in natural porous media using synchrotron X-ray microtomography: Environmental Science and Technology, **40**, 6622–6629, doi: 10.1021/es0602851.

Schwartz, N., J. A. Huisman, and A. Furman, 2012, The effect of NAPL on the electrical properties of unsaturated porous media: Geophysical Journal International, **188**, 1007–1011, doi: 10.1111/j.1365-246x.2011.05332.x.

Schwarz, G., 1962, A theory of the low-frequency dielectric dispersion of colloidal particles in electrolyte solution: Journal of Physical Chemistry, **66**, 2636–2642, doi: 10.1021/j100818a067.

Sen, P. N., 1981, Relation of certain geometrical features to the dielectric anomaly of rocks: Geophysics, **46**, 1714–1720, doi: 10.1190/1.1441178.

Sen, P. N., C. Scala, and M. H. Cohen, 1981, A self-similar model for sedimentary rocks with application to the dielectric constant of fused glass beads: Geophysics, **46**, 781–795, doi: 10.1190/1.1441215.

Shefer, I., N. Schwartz, and A. Furman, 2013, The effect of free-phase NAPL on the spectral induced polarization signature of variably saturated

soil: Water Resources Research, **49**, 6229–6237, doi: 10.1002/wrcr.20502.
Slater, L. D., and D. Lesmes, 2002, IP interpretation in environmental investigations: Geophysics, **67**, 77–88, doi: 10.1190/1.1451353.
Sutherland, J. W., and J. W. T. Spinks, 1959, Radiolysis of tetrachloroethylene: Canadian Journal of Chemistry, **37**, 79–90, doi: 10.1139/v59-013.
Titov, K., A. Kemna, A. Tarasov, and H. Vereecken, 2004, Induced polarization of unsaturated sands determined through time domain measurements: Vadose Zone Journal, **3**, 1160–1168, doi: 10.2136/vzj2004.1160.
Titov, K., V. Komarov, V. Tarasov, and A. Levitski, 2002, Theoretical and experimental study of time domain-induced polarization in water-saturated sands: Journal of Applied Geophysics, **50**, 417–433, doi: 10.1016/S0926-9851(02)00168-4.
Turner, M. L., L. Knüfing, C. H. Arns, A. Sakellariou, T. J. Senden, A. P. Sheppard, R. M. Sok, A. Limaye, W. V. Pinczewski, and M. A. Knackstedt, 2004, Three-dimensional imaging of multiphase flow in porous media: Physica A: Statistical Mechanics and Its Applications, **339**, 166–172, doi: 10.1016/j.physa.2004.03.059.
Ustra, A., L. Slater, D. Ntarlagiannis, and V. Elis, 2012, Spectral induced polarization (SIP) signatures of clayey soils containing toluene: Near Surface Geophysics, **10**, 503–515, doi: 10.3997/1873-0604.2012015.
Vanhala, H., 1997, Mapping oil-contaminated sand and till with the spectral induced polarization (SIP) method: Geophysical Prospecting, **45**, 303–326, doi: 10.1046/j.1365-2478.1997.00338.x.
Weller, A., L. Slater, S. Nordsiek, and D. Ntarlagiannis, 2010, On the estimation of specific surface per unit pore volume from induced polarization: A robust empirical relation fits multiple data sets: Geophysics, **75**, no. 4, WA105–WA112, doi: 10.1190/1.3471577.
Wildenschild, D., and A. P. Sheppard, 2013, X-ray imaging and analysis techniques for quantifying pore-scale structure and processes in subsurface porous medium systems: Advances in Water Resources, **51**, 217–246, doi: 10.1016/j.advwatres.2012.07.018.
Willson, C. S., R. W. Stacey, K. Ham, and K. E. Thompson, 2004, Investigating the correlation between residual nonwetting phase liquids and pore-scale geometry and topology using synchrotron X-ray tomography: Proceedings of SPIE, **5535**, 101–111, doi: 10.1117/12.560545.
Yang, C., T. Dabros, D. Li, J. Czarnecki, and J. H. Masliyah, 2001, Measurement of the zeta potential of gas bubbles in aqueous solutions by microelectrophoresis method: Journal of Colloid and Interface Science, **243**, 128–135, doi: 10.1006/jcis.2001.7842.
Zhang, Z., S. Kruschwitz, A. Weller, M. Halisch, and C. Prinz, 2017, Enhanced pore space analysis by use of μ-CT, MIP: Proceedings of the Annual Symposium of the Society of Core Analysts, Extended Abstracts, SCA2017–086.
Zimmermann, E., A. Kemna, J. Berwix, W. Glaas, H. M. Münch, and J. A. Huisman, 2008, A high-accuracy impedance spectrometer for measuring sediments with low polarizability: Measurement Science and Technology, **19**, 105603, doi: 10.1088/0957-0233/19/10/105603.
Zisser, N., A. Kemna, and G. Nover, 2010, Relationship between low-frequency electrical properties and hydraulic permeability of low-permeability sandstones: Geophysics, **75**, no. 3, E131–E141, doi: 10.1190/1.3413260.